DEPARTMENT OF
ATMOSPHERIC SCIENCES

UNIVERSITY OF WASHINGTON

FIRST ANNUAL REPORT
on Contract NASA NsG-632

On the use of Intermediate Infrared and Microwave Infrared in Weather Satellites

by

KONRAD J. K. BUETTNER
KRISTINA KATSAROS
WILLIAM KREISS

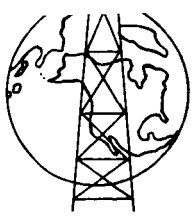

September 1965

Prepared for
National Aeronautics and Space Administration
Goddard Space Flight Center
Greenbelt, Maryland

DEPARTMENT OF ATMOSPHERIC SCIENCES

University of Washington

First Annual Report

on Contract NASA NsG-632

On the use of Intermediate Infrared and Microwave Infrared in Weather Satellites

by

Konrad J. K. Buettner

Kristina Katsaros

William Kreiss

September 1965

Prepared for

National Aeronautics and Space Administration
Goddard Space Flight Center
Greenbelt, Maryland

TABLE OF CONTENTS

Introduction

This study tries to open new ways for the use of weather satellites and other remote control observations. Items investigated range from the newly discovered emissivity or albedo variations in the 4μ window over surface temperature problems with the 10μ window to the construction of a 18 Gc/s radiometer for the cm-window.

Note: All temperatures given below are in degrees Kelvin except when mentioned otherwise. "Hot" or "cold" means HRIR received signals which are higher or lower than the reference which, as a rule, is the environment.

The 4μ Window, Observations of Albedo

A glance at the HRIR 4μ pictures of Nimbus I reveals a remarkably sharp separation of water and land. This holds for day and night pictures. One could say, of course, that in a September night all waters are warmer than the land and vice versa at daytime. On closer sight, however, things are more complicated. The effect of temperature contrasts seems enhanced by sun's reflection at daytime and local variations of emissivity at night.

To investigate the 4μ albedo from Nimbus daytime data we assume that the reflectivity is gray and diffuse within the filter area. This is, of course, a guess and verification can come only from detailed spectral experiments. This is certainly not the case for the soil of the Pawnee National Grasslands in Colorado (1a). We call

ε the emissivity

$(1 - \varepsilon)$ the albedo

T_R the true surface temperature

T_N the temperature taken from Nimbus HRIR data

B the black body emission for the spectral area, direction and temperature involved

τ_1 the transmissivity of the beam sun to surface area

τ_2 the transmissivity surface area to satellite

z the solar zenith angle

S the reflected solar irradiance for our spectral area (watt cm^{-2} $ster^{-1}$), i.e., the irradiance found above an atmosphere-less earth of 100% diffuse albedo.

We have then,

$$\tau_2 \cdot \varepsilon \cdot B(T_R) + \tau_1 \cdot \tau_2 \cdot \cos z \cdot (1 - \varepsilon) \cdot S = B(T_N) \qquad (1)$$

Assuming first $\tau_1 = \tau_2 = 1$ we find

$$\varepsilon = \frac{S \cdot \cos z - B(T_N)}{S \cdot \cos z - B(T_R)} \qquad (2)$$

S can be found by assuming a solar constant of 2.0 cal cm^{-2} min^{-1} and a solar spectral distribution like that of a 6000°K body. From this we find S = 1.30 watt cm^{-2} $ster^{-1}$ corresponding to 350°K blackbody emission. Obviously if T_N or T_R approach this temperature eq. (2) becomes useless.

Tentative ε data were evaluated from a few daytime passes. Flight 195/6 leads near local noon over a line: W. Cuba-Panama Canal-Cape Horn. The gray scale used for the positive film prints deviates by about 40°K from the one given on page 93 of the Catalog (1b). Calibration of the scale for this flight can be taken from the Carribean Sea (300°K) for the north part of the film and from the Pacific near 30°S for the southern part. A second check point cannot be found on these pictures since ε is unknown for all surfaces except water where it is near unity. Since true data are not available yet we may guess at the values of the gray scale. Above 255°K the scale in the Catalog (1b) doubles the intensity for each single step or

$$b_x / b_{x-1} = 2.0 \qquad (3)$$

if x = 1, 2, 3 are the numbers of the scale for 255°K and more and b the corresponding $B(T_N)$.

If we presume that this law holds also for a scale shifted by four points, the average T_N change would increase per scale step from 15°K at

295 to 20°K at 340°K. We could, on the other hand, take the average increase of the Catalog from 250 to 310°K as 12°K per step and extrapolate this to 350°K. We selected the latter more conservative figure to estimate T_N data.

The Orinocco river shows clearly at about 5°N, 68°E. Its T_N coincides with that of the ocean. A temperature of 300°K seems quite typical for such a broad jungle river. T_N for some areas around is obviously higher. The geographic outline is distinct enough to exclude clouds over most of Colombia and Venezuela. A "hot" area lies south of the Gulf of Uraba; this seems to be the very wet jungle of the west slope of Cordillera Occidental. This jungle has a T_R very close to 300°K since according to (2) this is the average temperature of tree tops in this climate. Very little change for time of day, season, or tree height was observed. These jungles show not a trace of soil to the satellite.

Other areas in Colombia could not be evaluated since no forestry or climatic data are available. However, the "hot" areas of northern Guyana, the area south of Lake Maracaibo and the coastal stretch around Caracas could be located on an excellent forest map of Venezuela. All three regions are jungles, free of people and steppes. The T_R again cannot deviate much from 300°K. The "hottest" spot on the picture is the coastal desert of Guarjira and two obviously cumulus type clouds north of Colombia. Guarjira could of course be quite hot; but on the other hand, desert quartz sand is expected to have some albedo. The cumulus clouds could be some 10 or more degrees below the sea temperature of 300°K. Finally, the hurricane Dora clouds are very cold on top, making their $B(T_R)$ insignificantly small.

Clouds seem to have very different albedos. Compare:

1) Run 175, daytime, area 50-60S, 68-80E at 07:13 GMT, 9 September, 1964

2) Run 181, night, same area at 18:43, GMT, 9 September, 1964

The second picture shows a front starting at about 70°S, 90°E going to 50°S, 80°E. We see a moderately "cold" area ahead, probably a cirrus with the ocean radiating through. Then comes a very "cold" wing, obviously altostratus. Behind the front are many scattered small "cold" areas obviously cumuli in instability showers. Now in the day pictures only 11 hours prior the cirrus area cannot be found. The altostratus is now "hot," its T_N close to that of the ocean. The cumuli, however, are clearly there, albeit somewhat "warmer" than their brethern in the same picture at about 40° 220E.

More daytime cloud data: Run 195/6 shows a large cloud over Panama with a "hot" core and a "cold" core periphery. More such "cold" clouds are seen over the whole range of the sun glare. The big Panama system seems to be cirrus in the center and normal cumulus at the periphery.

Run 206 shows "cold" clouds over Southern Spain, Northwest France and Northwest Africa. It also shows a "hot" cloud south of Marseille.

To evaluate correct albedo data from these areas we have to wait for the direct read-out data. Present estimate is:

albedo altostratus -- 10%

albedo cumulus -- 4%

Runs 174, 175, and 206 show the albedo of Antarctica to be also quite substantial.

Night data may also be used to find ε. Run 229 on 23:47 GMT of 12 September 1964 gives good coverage of north and central Europe down to

the Ahaggar Mountains in the Sahara.

1) From climatic data and on-shore wind the surface temperature of the Southern Gulf of Bothnia is 281°K, that of the Mediterranean, 295°K. The gray scale of the two areas fits very well with these data.

The area of the southern parts of Bavaria, Wuerttenberg and Baden reports exactly two minutes before Nimbus flight an average screen level temperature of 288° (ten stations). Data vary from 14°C (Ulm) to 17°C (Karlsruhe), Nimbus data, however, show the T_N of Bothnia about one scale or 15° "hotter than Southern Germany.

2) The Ruhr area can be seen to be markedly "hotter" than its environment. There is no orographic reason discernible for this fact. The screen temperature taken from the daily German map as well as from a letter of Dr. Klug, Weather Bureau at Essen, indicates an average (six stations) of 283°, that of areas adjacent to all four directions about 281°, an insignificant difference. Four possible reasons for the T_N difference of the Ruhr vs. its environment are considered:

a) The Ruhr surface temperature deviates less than that of the environs from the screen temperature. Only tests could show whether this makes sense.

b) There could be an industry caused warm blanket of smog over the Ruhr, held in space by a good inversion. This air would emit "warmer" than the ground. This inversion-smog combination, however, is excluded by the observations; the inversion is 100 m high, 1° warmer than surface air, very dry (50% relative humidity), visibility is 15-30 km and no smog.

c) The Ruhr radiation could be caused by open heat sources such as chimneys and their effluents, open fires, etc. Emission of a black body at 600° would be about 300 times, at 900° about 6000 times stronger than that of a 300° body of equal area. To raise T_N from 280° to 290° or from 0.085 to 0.133 watts m^{-2} $ster^{-1}$ would require that

$$(1 - \alpha) \cdot 0.085 + \alpha \cdot b \cdot 0.085 = 0.133 \qquad (4)$$

where α is the relative area covered by a hot source emitting b times more than 0.085 watts. With b = 6000 (for a 900° source) we find $\alpha \approx 10^{-4}$. An area of 10 x 10 km^2 should then contain a fire area of 10^4 m^2 or 100 x 100 m^2. The temperature of 900° is that of a typical open wood or gasoline fire (7). The fire area mentioned seems rather unrealistic. It might be noted also that all bits of information from the Ruhr are higher by the same amount. There is no single "hot" spot.

This simple calculation shows also the limitations of Nimbus HRIR for spotting forest fires.

d) The Ruhr area could have a higher ε than the environs which are covered with soil or vegetation, whereas the Ruhr which is infamous for its air pollution might be covered with a thin layer of soot. There has been no measurable amount of precipitation for two days before.

3) The Sahara shows two distinctly "hot" areas, namely the Ahaggar Mountains and the Djebel Garian south of Tripolis (Runs 229 and 258). Both areas contain steep slopes with little chance for sand or dust to adhere. Vegetation is minimal. Temperature minima in the Ahaggars decline with

altitude (5). So these mountains should be "cold" not "hot." Maybe the absence of quartz sand causes the slopes to show the ε of solid rocks which ought to be high.

An interesting area is north of lat. 24-27° N 11°E. This is "hot" at daytime (run 206/7) and also "hot" at midnight (run 258). It is listed as true desert. It might be hot as well as reflecting.

Theory of Albedo

Visible albedo is essentially composed of

1) Specular albedo on ice, rocks, water, metals and other surfaces

2) Diffuse albedo from finely dispersed matter which is somewhat permeable to the visible. Examples are snow, sand, clouds, foam, and powders of NaCl, MgO, etc.

3) Specific molecular albedo such as that of chlorophyll.

10μ albedo is essentially caused by residual rays of quartz and other compounds of Si and O. Specular albedo may reach near 100% in these rays. But items 2) and 3) of above are unlikely to contribute since most substances are impermeable. The permeable NaCl as a powder, however reaches a 50% albedo.

The 4μ albedo should be somewhere in between the visible and the 10μ area. NaCl, KCl and similar salts should, in dispersion, give very high albedoes. To make estimates on other substances we first consider specular albedo of solids and liquids. Water and ice reflect about 2% for vertical incidence and more for other angles. Data for rocks are equally low as far as we know.

For disperse matters such as clouds, sand, dust and snow we have to consider the absorptivity, reflectivity, wavelength, and typical particle

diameter. For convenience we introduce d(1/2) as the depth in which a 4μ ray is halved by absorption. Some examples are (see Table 1);

1) Dune sand. Quartz particles of 100μ diameter are large compared to λ and d(1/2) exceeds 1000μ. Albedo will be high, maybe 30%. Geometrical optic applies.

2) Dust or soil of carbonates. Particle diameter may be equal or smaller than λ and also than d(1/2). Laws of fine particle scattering apply. Albedo can be substantial.

3) Water clouds. Particles are larger than λ and d(1/2). In each step a large fraction is absorbed. Albedo should be low.

4) Ice clouds, snow. Whereas reflection and transmission in the solid is poorer than in water, effective particle diameters might be very small. Albedo should be moderate.

5) Green leaves reflect little in the visible, about 50% in the near IR, very little at 10μ. One single test at 4μ shows a 15% albedo (8). Vegetation might be quite reflective.

TABLE 1. Penetration of 4μ rays in homogenous material and type of dispersing matter.

Material	50% Depth, d(1/2)	Dispersion Diameter	Type
Ice	25μ	10μ	Cirrus
Water	50μ	10-40μ	Cumulus
Quartz	1300μ	100	Dune
Feldspar	180μ	100	Dune
$CaCO_3$	65μ	<10	Dust, soil
$MgCO_3$	40μ	<10	Dust, soil

Daytime 4μ data might help to differentiate: type of clouds, type of vegetation, type of soil.

If a 10μ radiometer is used concurrently, surface temperature and albedo can be found.

The 10μ Window

Our first effort in evaluation of satellite temperature measurements by use of the infrared centered on determination of emissivities in the 8-12 micron window for surfaces on the earth. Field measurements of emissivity were obtained in Eastern Washington and in Death Valley with the "emissivity box" (9). Results of field and laboratory tests were tabulated in the semi-annual report of this contract. In summary we may state that: in order for the earth to show a significant deviation from "blackness," it is necessary that the top surface be free of vegetation or even humus. In the Eastern Washington studies it was found that for the Ginko area almost all surfaces showed very high emissivities, around 99%. As we progress east and southward to the drier area of Hanford, there was obviously much less vegetation, no leichen to speak of on the rocks, and here the emissivities ranged from 94.6% for a quartz sanddune to 98.5% for a very fine lava silt.

For the Death Valley-Amargosa Desert area, where we have even less vegetation, deviation from blackness up to 10% was found for certain silicious rocks. Most of the lava rock types had emissivities of 96-99%.

Since the temperature regime in Death Valley had become of concern through the Nimbus I HRIR photos the interest focused on the special features of the valley such as the salt pools. For 8-12 micron the salt emissivity

as measured in the field gave 97.6%. At home in the laboratory tests were made on NaCl for emissivity. As the size of NaCl crystals was decreased through grinding the corresponding emissivity also decreased. For 2-5 mm crystals the emissivity was 98.8% and for the same ground to a few hundred micron grains it was 85%, while for reagent NaCl the emissivity was as low as 57.0%.

Since NaCl is highly transmissive in the infrared, as snow is to the visible, we may have similar diffuse reflection occuring for the two materials in different wavelength bands. We are now intrigued by a possible similar effect of grain size for quartz at 4 microns, where this material is transmitting.

Field Work on Radiative Surface Temperatures and Sky Temperature

During the summer 1965 we have been out in the field obtaining radiative temperatures of various surfaces over 24 hour periods, and also sky temperatures as a function of zenith angle around the clock. For both purposes we have used the Barnes IT2 Infrared Thermometer with 8-12 micron filter, and cavity temperature at 52°C. In order to measure sky temperatures, which for this wavelength region and summer time give effective black body temperatures of down to -40°C in the zenith, we affixed a bucking potential, using a very fine variable resistance of 8000-9000 ohms, and regular 3 volt battery. Calibration for this low temperature range was done by using propyl alcohol baths cooled by solid CO_2. Propyl alcohol has practically 100% emissivity at 8-12 microns as measured with our emissivity box, and by stirring well we hope to have obtained a good calibration. In the 0-50°C range water baths were used for calibration. Emissivity of water is also very high. At each measurement in the field check points were obtained for an icebath and a

water bath at 15° to 20°C. We had car batteries for our power supply, and since the Barnes is sensitive to the power and somewhat to environmental temperatures this proved a very valuable checking procedure.

Radiative Surface Temperatures

On July 15-16, 1965, the Barnes was set up on the north side of the Stevens Canyon in Mount Rainier National Park. This observation point was chosen because spruce thickets, deciduous low growth, a rock slide and rock faces, as well as snow fields and green meadows could easily be sighted here, and some surfaces under high declination angles, thus best simulating the satellite observation point. Stevens Canyon runs N.W. to S.E. with a rise from 900 to 1950 m. We were at 100 m above the canyon floor. The tested areas were in the bottom of the canyon and on the north-facing slope. We also observed a west facing and a south facing rock wall on the northern ridge of the canyon. The weather was clear and with slight gradient winds, except for the early morning hours on July 11, when a stratus deck hovered over the canyon. Valley and slope winds were noted. Maximum-minimum thermometers were set out in areas also observed with the Barnes. In the following graphs emissivity deviations from blackness has not been corrected for, neither has atmospheric interference been considered. For the curves presented the optical paths are approximately equal, and the real distances are small, of the order of a few hundred meters at the most. Measurements were also taken of more distant objects, but here it is obvious that the atmospheric influence has to be corrected for. Snow fields about 3 km away, for instance, show equivalent black body temperatures of 10°C.

The surfaces of Fig. 1 are more or less horizontal and in the bottom

of the canyon, thus their maximum temperature occurs near local noon. The differences between their temperatures are due to their differences in solar absorption and heat conductivity rather than exposure.

In Fig. 2 we see that the maximum occurs about three hours later for the west facing rock wall than for the south facing one, but the maximum temperature reached is almost identical. In the morning the south face starts warming two hours or so earlier than the west face as expected. The northeast facing slide above the river has an early morning warm-up, and reaches its maximum at 9 a.m., and then cools off.

The maximum thermometer in the spruce thicket showed about 21°C at 1.3 m above ground near a tree trunk, while the radiative maximum temperature of the tree tops was 25°C. This gives a 4° temperature difference crown to ground. A maximum thermometer placed in shade above the rockslide, showed 25° while the sunlit rockslide has a maximum temperature of 30°C. The minimum thermometer readings coincided to within a degree with the minimum of the radiation temperature curves. This agreement is undoubtedly due to the early morning overcast.

Also in Mount Rainier National Park, but in the northwest corner at Ipsut Pass, we took similar measurements as in Stevens Canyon. We wished to measure the temperature gradient down the forested slopes of the north ridge of the Carbon River valley. The diurnal wind system of this valley has been thoroughly investigated by this department (10). Carbon Valley at observation point runs N.W. to S.E., and we looked at it from a pass in the ridge to the south through a small side valley.

During the night we unfortunately had a sudden northerly gradient wind

up to 15-20 knots for a few hours, which obliterated radiative differences, but during the daytime hours we see a temperature difference of 2-3°C between top and bottom of this north rim of the valley. No corrections for atmospheric influence has been applied here either as yet, but the slope is steep, having a 900 m rise in 1800 m horizontal distance, so the atmospheric influence should not vary much from top to bottom.

From Ipsut Pass we also observed the temperature regime of low green growth, spruce thickets and rockfaces. The graphs are presented in Fig. 3. We may note that the darker spruce tops are ~~warmer~~ cooler by day and ~~cooler~~ warmer by night than the lower and lighter colored deciduous growth.

From the roof of a building on the University of Washington campus we observed temperatures of various surfaces such as concrete and brick walls, a mudflat and large chestnut trees (see Fig. 4). The north and south facing concrete surfaces were not vertical, but made an obtuse angle with the horizontal. The brick wall was vertical. The chestnut tops were observed at an angle from the east, and the mudflats from the west. For these latter two an atmospheric correction may be necessary

Sky Temperature Measurements

During July 28-30, 1965, Seattle had clear warm days and nights due to an upper level ridge. With the equipment on top of the campus building sky temperatures were observed for 36 hours. Some of the data are presented in Figure 5. A diurnal shift on the temperature scale is noticeable for these curves, but the results are not definitive.

The following formula of sky radiation as a function of zenith angle was found by Strong (12) to fit the data of Dines, which included the whole

spectrum:

$$I_\theta = a + b \sec^{1/2}\theta \qquad (5)$$

I_θ is radiant emittance

θ is zenith distance

a and b are empirical constants

Also in his spectroscopic studies of infrared sky radiation for various wavelengths Strong found the $\sec^{1/2}\theta$ type plot (eq. 5) to give a better fit than the Langley plot of sec θ versus the logarithm of emittance (12). The latter formula is based on Beer's law in that the path length increases proportional to the sec θ.

The secant dependency of the logarithm of emission is an indication of continuous absorption for the wavelength interval, while the $\sec^{1/2}\theta$ dependency according to theoretical work by Ladenburg and Reiche (13) and others is expected for the overall absorption by a band of strong lines. In the 1941 work by Strong he makes a case for strong band type absorption in the "window" based on his own data and data obtained by Adel against a continuous absorption as predicted by Elsasser. In his later work, Elsasser (1960) develops the absorption by a spectral line, and discusses the special cases of strong and weak absorption (14). For a weak line he finds its atmospheric absorption to be linearly proportional to optical depth, u. However, for a strong line the center part is completely absorbed in a short distance, and further absorption takes place in the wings, and is proportional to the square root of optical depth, $(u)^{1/2}$ and hence to $\sec^{1/2}\theta$. The absorption in the 8-12 micron "window" is mainly due to wings of water vapor lines having their centers outside the window, and to some weak transitions. The ozone absorption band at 9.6 microns is strong

and would also point to a $\sec^{1/2}\theta$ relationship between sky emission and zenith distance.

A small computer program was written to fit various types of curves to the data. The two curves $I_\theta = a + b \sec^{1/2}\theta$ and $I_\theta = a_1 + b_1 \sec\theta$ were tried. With a change of variable $\sec^{1/2}\theta = u$ and $\sec\theta = v$ linear regression formulas can be used as expressed by Panofsky (14). In order to see which formula gave the best fit, the "goodness of fit" was calculated by the formula:

$$S_{21} = \frac{\sqrt{\Sigma(\tilde{I_\theta} - I_\theta)^2}}{N} \qquad (6)$$

where $\tilde{I_\theta}$ is the emittance value predicted by the curve, and I_θ is the observed value for the same zenith distance. S_{21} is called the scatter and N is the number of data points. The radiation data were averaged over three hours for each even 5 degrees of zenith distance. For 9 such sets of data obtained during July 28-30 the secant curve had 3 to 4 times the scatter of the $\text{secant}^{1/2}$ curve. The emittance was in watt/m^2 as computed by an integration of the Planckian over the 8-12 micron window for the equivalent blackbody temperature given by the Barnes instrument.

The curve $\ln I_\theta = a + b \sec\theta$ was also fitted for both natural logarithm and for logarithm to the base 10. The scatter is the same for both curves, which is obvious since $10 = e^y$ or $e = 10^x$. For the 9 cases the scatter of these curves was 5-10 times larger than the scatter for the curve expressed by eq. 5.

Linke has used a formula $L_\theta = L_0 \cos^r \theta$ for the heat loss under an angle from a horizontal black instrument (15). L_θ is the loss at an angle θ and L_0 is the loss to zenith. θ is again zenith distance and r is an empirical

constant to be found. Since we have data for the incoming sky radiation rather than the net outgoing I tried to find an R that best fit the data to the formula

$$I_\theta = I_0 \sec^R \theta \qquad (7)$$

Angular variation of net outgoing radiation

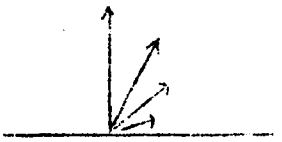

Angular variation of incoming sky radiation

The equations are not simply comparable since Linke's formula of course includes a term K for the outgoing infrared radiation from the earth's surface. If we assume the earth to be black K is not a function of θ and we can then write

$$L_\theta = (K - I_\theta) \qquad (8)$$

Results of fitting the curve of eq. (7) gave values of R ranging from 0.29-0.51. The scatter was of comparable magnitude to that of eq. (5). Six of the nine cases had an R close to 0.5.

Conclusion

It seems that for the 8-12μ window the angular variation of incoming sky radiation can be well represented as a linear function of $\sec^{1/2}\theta$.

The cm Window, The Construction of an 18 gc/s Radiometer

In this part of the report details of the radiometer design will be elaborated upon. Contrary to the optimistic view taken in the first semi-annual report (April, 1965) regarding the time schedule for completion of this instrument there still remain several important tasks before meaningful quantitative observations can be obtained. These tasks will be mentioned in the course of the following discussion.

Figure 6 is a view of the completed radiometer in the configuration for sky and cloud observations. It is well to point out at this time that the instrument is by no means "state of the art" in either size or components. It was built in the manner illustrated in order to utilize readily available components and to permit easy modification. At a later date when aircraft observations come into consideration the circuit design should be finalized permitting more compact packaging. For the time being the cabinet houses some rather bulky power supplies and provides a sturdy support for the antenna assembly.

As was stated in the semi-annual report the intention has been to keep the radiometer as simple as possible. In choosing a total power radiometer simplicity in terms of circuit complexity is certainly achieved, but at the expense of having to cope with stability problems. For the purpose which this instrument is being constructed rms output fluctuations of 1-5°K are thought to be acceptable, considerably easing the requirements on gain stability, temperature control and local oscillator stability. The main problem encountered has been an excessively long "warm up" time required to minimize drift.

In Figure 7 is shown a block diagram of the radiometer. Each block is labeled in some detail so that thorough discussion of all blocks need not be made. For the most part, design of the radiometer has centered about the microwave "front end" and for this reason Figures 8, 9, and 10 are included to show details which will be discussed below.

The antenna is a fibre-glass parabaloid 1.07 meters in diameter fed by a 10 db horn. The paraboloid has previously been used in a 32 gc/s microwave communication link so that its surface accuracy is suitable for use at 18.8 gc/s. However, its original silvered surface was badly chipped so that it has been sprayed with aluminum. The focal length to diameter ratio is 0.33 and the Rayleigh distance is 150 meters. Using the following empirical formula for parabolic reflectors illuminated by small horns (17).

$$G = \Gamma_E + \Gamma_H + 10 \text{ Log } \frac{\pi d^2}{4\lambda^2} \qquad (9)$$

the gain G is calculated to be 45.1 db. In this formula Γ_E and Γ_H are factors dependent upon the attenuation at the edge of the reflector in the plane of polarization being considered, d is the diameter of the reflector and λ is the wavelength. The attenuation at the edge of the reflector is obtained from the manufacturers specifications for the horn and Γ_E and Γ_H are tabulated by Thourel. Using this gain figure the approximate half power beamwidth is calculated to be 1.02 degrees. One of the remaining tasks is the accurate boresighting of this antenna and measurement of its gain and radiation pattern. For boresighting provision has been made for adjusting the positions of both the reflector and the feedhorn with respect to each other. Polarization of the antenna can be changed by rotating the entire

microwave assembly in its supporting yoke. Figure 9 is a front view of this antenna.

Referring to Figures 8 and 10 the major components of the microwave "front end" can be identified. The local oscillator is a 2K25 klystron housed in the large cylinder followed by a solid state frequency doubler providing 5 mw at 18.8 gc/s. This power is coupled through an attenuator and absorption wavemeter to the balanced diode mixer. An AIL type 1354132 integrated mixer and solid state 30 mc/s preamplifier is employed and is packaged in the long rectangular box. For calibration purposes a Demornay-Bonardi type 2140 waveguide mounted "noise" diode is fed through an attenuator and 10 db directional coupler to the signal input port on the mixer. This "noise" source is connected at all times and, as such, contributes an excess "noise" temperature T_{NE} given by

$$T_{NE} = \frac{T_D - T_o}{L_c L_A} \qquad (10)$$

where T_o is the ambient temperature, T_D is the effective noise diode temperature, L_C is the fixed coupling loss and L_A is the attenuation (18). For large values of L_A the calibration circuitry contributes about 30°K to the receiver noise temperature. The range of calibration temperatures with this arrangement is approximately 30-1100°K and permits establishing calibration increments. When the antenna input is switched to a known "cold source" the radiometer can be calibrated absolutely to an accuracy dependent upon the accuracy to which the "cold source" and T_{NE} are known. A scheme for achieving this absolute calibration has been devised but not yet incorporated.

The center frequency of the preamplifier is 30 mc/s and its 3 db bandwidth

is 8 mc/s. The post-amplifier, an AIL type 130 laboratory receiver, has a 3 db bandwidth of 3 mc/s which will be increased to 8 mc/s to match that of the pre-amplifier. The detector is a crystal diode operating in a linear mode with its time constant selected by switching the integrating capacitor and its output is fed to a servo recorder through a balancing network, which is required to establish the "reference zero level." The recorder shown in Figure 6 is a Varian 10 mv model which will soon be replaced by a more versatile Moseley model 680 5 mv recorder.

The applicable radiometer formula is

$$\Delta T = M\,(T_A + T_R)\,(B\tau)^{1/2}\delta \qquad (11)$$

where ΔT is the rms output fluctuation, M is a mode factor, T_A the antenna temperature, T_R the receiver temperature, B is the pre-detection bandwidth, τ the integration time constant and δ an instability factor (19).

For the two channel total power radiometer the proper mode factor is M = 1. Assuming that the overall noise figure of the receiver is 12 db a receiver noise temperature of approximately 3400°K is obtained. Letting T_A = 300°K, δ = 1, B = 3 mc/s and τ = 1 second the calculated rms fluctuation ΔT is found to be 2.1°K. Laboratory tests yield a value for ΔT of about 5°K with approximately these parameters. The discrepancy lies both in the accuracy with which the parameters are known and in the instability factor δ which certainly cannot be unity. When the bandwidth of the post-amplifier is increased to 8 mc/s the output fluctuations should be reduced by $\sqrt{8/3}$.

In summary, a microwave radiometer has been built which appears to satisfy

the desired performance specifications. However, a number of important tasks remain to be completed. These are:

1. Boresighting of the antenna and determination of its gain, main lobe beamwidth and radiation pattern.
2. Broadening the post-amplifier bandwidth to 8 mc/s to match that of the pre-amplifier.
3. Absolute calibration of the radiometer and accurate determination of the output fluctuations.

These tasks will be carried out as expediently as possible to permit initiation of an observation program.

In the preceeding discussion many of the troublesome subtleties which have been encountered have purposely been omitted. The intention has been only to outline the general characteristics and configuration of the instrument. In the following discussion some of the uses for this radiometer will be outlined.

Some Proposed Uses of the Microwave Radiometer

The radiometer configuration shown in Figure 6 is intended primarily for observations of sky temperature under various degrees of cloudiness and for detailed study of large scale thunderstorm cells. It may also be used for measurement of the effective emissivity of surface features such as forests, mountains, and bodies of water at distances greater than the Rayleigh distance and near grazing angles. If taken into nearby mountains some of these measurements can be obtained at near normal incidence. Such measurements with a similar radiometer configuration have been made and reported at 35 gc/s (20).

As was mentioned in the semi-annual report two antennae are provided

for the radiometer described above. By removal of the parabaloid and feedhorn and replacement with a small 20 db horn antennae small samples of various materials can be studied. In order to minimize the proximity effects of the radiometer the plate upon which the microwave section is mounted can be supported on a small tripod and the horn antenna directed parallel to this plate towards the sample. It is also likely that a circulator and/or an isolator would be required between the antenna and the input port of the mixer to minimize reflection of radiated local oscillator power. The material samples can be supported in such a way that the angle of incidence can be varied from normal to grazing. This last arrangement is termed the configuration for surface emissivity measurements and has not yet been implemented. However, similar measurements at 16 gc/s have been reported (21).

At a later date it may be possible to carry out a series of observations from an aircraft. Within reasonable distance of Seattle are found many representative surfaces which will be viewed by a satellite born radiometer; from desert to glaciers and salt water to fresh water. With a nadir pointed radiometer a significant quantity of surface data can be collected from a light aircraft on relatively short flights.

Regarding the study of thunderstorm cells, the midwest during the summer months offers a good opportunity. It is required that the chosen location have a rain gauge network and a precipitation radar would be highly desirable. At the present time tentative plans are being laid for an excursion to a suitable area during the summer of 1966.

Considerations Relevant to cm Wave Study

The purpose of the present study is to examine the feasibility of obtaining additional useful information for weather reporting and forecasting through the inclusion of microwave infrared sensors in meteorological satellite payloads. Interpretation of the "pictures" obtained from such sensors is dependent upon knowledge of the geography of the sub-satellite point corresponding to the "picture" and of the "surfaces" being viewed. Complicating this interpretation are the lower resolution of the sensor (compared to optical and intermediate infrared sensors) and the depth of penetration of the microwave radiation (or the depth from which the radiation is considered to originate). The transparency of clouds is an advantage of this region of the spectrum only if the radiations arising from the "surface" and intervening atmosphere can be sorted out.

The emissivities of various terrain are then important factors in an analysis of the data received from a satellite born sensor. These emissivities in the microwave infrared region are functions of 1) the composition of the terrain, 2) its electrical conductivity, 3) its "roughness" and 4) the frequency of observation. In table 2 from (22) are listed some of the characteristics of different types of ground which have been obtained by direct and indirect means at lower frequencies. Because of the nature of the ground these must be considered as average or effective values. In the column labeled transition frequency is listed the frequencies above which the specified ground behaves as a dielectric. Intrinsic resistance is conductivity independent and the attenuation and apparent skin depth (not particularly meaningful) are dependent on conductivity but independent of frequency. There exists a range of frequencies above the transition frequency

TABLE 2. Characteristics of Different Types of Ground

TYPE OF TERRAIN	Relative Dielectric Constant $\varepsilon/\varepsilon_o$	Conductivity σ, mho/m	Transition Frequency $\frac{\sigma}{\pi\varepsilon}$, mc/s	Intrinsic Resistance $Z=(\frac{\mu}{\varepsilon})^{1/2}$ ohms	Attenuation $\alpha = 4.34\sigma Z$ db/m	Apparent Skin Depth $\delta = \frac{2}{\sigma Z}$, cm
Fresh water	80	10^{-3}	0.225	42	0.183	477
Sea water, minimum attenuation	81	4.64	1030	42	848	1.03
Pastoral, low hills, rich soil (typical of Dallas and Lincoln)	20	3×10^{-2}	27	84	11	79.3
Pastoral, low hills, rich soil (typical of Ohio and Illinois)	14	10^{-2}	12.9	101	4.38	19.8
Flat country, marshy, densely wooded (typical of Louisiana near Mississippi River)	12	7.5×10^{-3}	11.3	109	3.55	248
Pastoral, medium hills and forestation (typical of Maryland, Pennsylvania and New York, exclusive of mountainous territory and sea coasts)	13	6×10^{-3}	8.3	105	2.74	317
Pastoral, medium hills and forestation, heavy clay soil (typical of central Virginia)	13	4×10^{-3}	5.5	105	1.82	476
Rocky soil, steep hills (typical of New England)	14	2×10^{-3}	2.57	101	0.877	990
Sandy, dry, flat (typical of coastal country)	10	2×10^{-3}	3.6	119	1.03	840
City industrial area, maximum attenuation	5	10^{-3}	3.6	169	0.734	1180
City industrial area, minimum attenuation	3	10^{-4}	0.60	218	0.095	9170

where these conditions approximately hold, but in the microwave infrared region the characteristics of most materials have become frequency sensitive. This sensitivity results from the orientation of permanent dipoles and ionic or electronic conduction. In addition, the attenuation in some materials is temperature dependent.

Water has a high dielectric constant and high loss in the microwave infrared region and the properties of many materials are critically dependent on their water content. Thus, the differences in properties of some types of terrain may be almost entirely due to moisture content. In Figure 11 is shown the behavior of the dielectric constant of water at 3, 10 and 24 gc/s as a function of temperature (23).

The conductivity of water varies from 10^{-3} mho/meter for fresh water to about 6 mho/meter for sea water. Conductivity of the Great Lakes is about 10^{-2} mho/meter and is not highly variable. In the oceans conductivity is a function of temperature salinity and fresh water input and is considerably more variable. Regions of low temperature and high precipitation rate or large fresh water runoff have the lowest conductivity.

Within the continental United States the ground conductivity varies by a factor of 30. In general, hilly or mountainous regions are regions of relatively high conductivity. From a map produced by the FCC (24) it is seen that the lowest conductivities occur in the Colorado Rocky Mountains and the Sierra Nevada range. The highest conductivities occur in central Nebraska and North and South Dakota.

The behavior of emissivity as a function of the zenith angle for the earth's surface is of important concern largely because surface radiation represents the background against which phonomena taking place in the

atmosphere must be observed. One question which arises concerns the smoothness of the emissivity curves as a function of the zenith angle since many surfaces of interest are rough compared to the wavelength of observation. The Fresnel reflection coefficients apply to an element of surface but vary from point to point. Off hand, the problem appears to be similar to that of scattering of electromagnetic waves from rough surfaces and it is expected that the frequency dependence of emissivity is related to roughness also (26).

In figures 12 and 13 are shown a few emissivity measurements which were mentioned earlier. These results show the typical behavior of real materials in their departure from Lambert's law with the exception of the curve for water in figure 12 which is more typical of a conductor at near grazing angles than a dielectric. The authors suggest that the discontinuous shape may be related to the Brewster angle and the overall shape to strong sky reflection from the surface (the phenomenon of the Brewster angle is observed only when losses are small and occurs at an incidence angle of approximately 53 degrees only for vertical polarization).

One important feature to note is that there appears to be little departure of the emissivity from that of the zenith direction for zenith angles up to 30 degrees. There is some doubt about the "blackness" of the results in figure 12. During the course of this study similar observations will be made for comparison with the above and observations of others and the theoretical aspects of surface emissivity in the microwave infrared region will be investigated.

Sky observations can be placed in two categories: 1) observation of the microwave infrared emission expressed as apparent sky temperature as modified by various degrees of cloudiness, types of clouds and precipitation

and 2) microwave emissions generated by charge production, exchange and discharge mechanisms. Under the first category are measurements which are important because of their direct relationship to the liquid water and water vapor content of the atmosphere. It is important to know how sky temperatures vary with location, time, and zenith angle. Numerous observations over a wide range of frequencies have already been made by radio astronomers and propagation researchers for the purpose of assessing the atmospheric and cosmic contributions to unwanted noise. Although the number of locations is small assimilation of the more reliable data may prove helpful for interpretation purposes. A study of the effects of meteorological conditions affecting radio astronomy observations has been made at NRAO at 9 gc/s which shows the effects of cyclonic conditions and frontal activity on observed fluctuations (26). In figure 14 are shown the type of average sky temperature results expected (26) with the dotted curve drawn in to represent the approximate results for 18.8 gc/s (1.6 cm).

Of particular interest is the contribution of rain to the sky temperature for there seems to be some possibility of detecting it against certain surface background, particularly oceans (28). Referring to figure 14b it is seen that the sky temperatures are considerably higher under conditions of moderate rain as compared to clear sky conditions. This is, of course, expected from emitting properties of an absorbing medium. In figure 15 are shown the approximate limits of attenuation by rain as a function of frequency (29). In this same reference is a tabulation of the distribution of drop sizes versus precipitation rate which has been widely used for many years. For present purposes it is mentioned that the range of water droplet diameters

found in the atmosphere are approximately 10^{-4} to 10^{-2} cm for cloud droplets, 10^{-2} to 5×10^{-2} cm for drizzle drops and 5×10^{-2} to 4×10^{-1} cm for rain drops. These figures lead to a range of droplet size to wavelength ratios of 6×10^{-5} to 2.5×10^{-1} for a wavelength of 1.6 cm (18.8 gc/s). The size of the largest rain drops approaches a wavelength suggesting the relative importance of scattering as a loss mechanism for rain elements as compared to cloud droplets. A soon to be published paper (30) has considered this problem in detail by solving the equations of radiative transfer exactly but the lowest frequency for which apparent sky temperatures have been computed is 30 gc/s. As the theoretical problems associated with the interpretation of precipitation observations revolve around the relative effects of scattering and absorption it should be pointed out that the choice of 18.8 gc/s for this study is partly based on the theoretical determination of the extinction properties of rain elements at microwave frequencies (31).

During the course of this study a program of observations is also planned which is aimed at assessing the effects of clouds and precipitation on the apparent sky temperatures at 18.8 gc/s. In the Seattle area there are frequent opportunities for observing scattered showers and uniform widespread rain or drizzle but the high precipitation rates associated with large scale activity will be studied elsewhere.

In the second category of cloud observations it is not expected that microwave emission due to discharge mechanisms will be observed (except possibly very close to a large lightning stroke) because of the rapidly decreasing power spectrum with increasing frequency (32) and the use of relatively long time constants in the radiometer. The power spectrum of

charge exchange mechanisms is also apparently negligible at these high frequencies (33). Nevertheless, during observation of the large scale convective clouds indication of these mechanisms will be looked for.

Future Plans

This group plans to continue this work along the lines discussed above. Direct field testing in the 4μ area for albedos and surface temperature looks promising. A photo-conductive cell instrument with filters may be built to obtain measurements in the 4μ and 10μ windows. From these data albedo as well as surface temperature could be found. A field testing program for the cm region will soon be initiated.

Acknowledgments

Kristina Katsaros was very fortunate this summer in having as her assistant Bonnie Rose, a high school student from Oregon, who spent the summer at the University of Washington campus as a member of a National Science Foundation science institute. Her help, especially in obtaining the sky temperatures July 28-30, and subsequent data reduction is gratefully acknowledged.

On the Ipsut Pass expedition fellow University of Washington graduate students helped with the back packing of equipment and with measurements.

William Kreiss wishes to acknowledge the valuable assistance of Sam Antion in designing and fabricating the antenna assembly and procurement of many important parts of the microwave radiometer.

References

1a) Marlatt, W. E., The Measurement of the Surface Temperature of the Earth, Technical Paper No. 64, Department of Atmospheric Sciences, Colorado State University, Fort Collins, Colorado, January 1965.

1b) Nimbus I, HRIR Data Users Catalog, Vol. I.

2) Baynton, H. W., Hamilton, H. L., Scherr, P., and J. Worth, Temperature Structure in and above a Tropical Forest, Quart. J. Roy. Met. Soc., Vol. 91, pp. 225-233, 1965.

3) Hueck, K., Mápa de vegetation de la republica de Venezuela, Institute Forestal Latino Americo, Merida, Venezuela.

4) Geiger, R., The Climate Near the Ground, Harvard University Press, Cambridge, Massachusetts, 1965.

5) Dubief, J., Le Climate du Sahara, Vol. 1, Université d'Alger, Algiers, 1959.

6) Buettner, K. J. K., Einige Strahlungsmersungen in der Tripolitanishen Sahara, Meteor. Z., Vol. 50, 1933, pp. 484-493.

7) Buettner, K. J. K. and H. Kuhn, Climates of the German Theatres of War, German Aviation Medicine, Vol. II, Dept. of the Air Force, Washington, D. C., 1949.

8) Bell, E. E., An Atlas of Reflectivities of Some Common Types of Materials, Engineering Report, Contract AF 33(616)-3312, Ohio State University Research Foundation, 1957.

9) Buettner, K. J. K. and C. Kern, The Determination of Infrared Emissivities of Terrestrial Surfaces, J. Geoph. Res., Vol. 70, No. 6, March 1965.

10) Buettner, K. J. K. and N. Thyer, Final Report AF 19(604)720, Department of Atmospheric Sciences, University of Washington, 1962.

11) Elsasser, W. M., Heat Transfer by Infrared Radiation in the Atmosphere, Harvard Meteorological Studies No. 6, Harvard University, Blue Hill Meteorological Observatory, Milton, Massachusetts, 1942, pp. 92-94.

12) Strong, J., Study of Atmospheric Absorption and Emission in the Infrared Spectrum, J. Franklin Inst., V. 232, p. 1, 1941.

13) Ladenburg, R. and F. Reiche, Uber selektive Absorption, Ann Physik, Vol. 42, p. 181, 1913.

14) Elsasser, W. M. and M. R. Culbertson, Atmospheric Radiation Tables, Meteor. Monographs, Vol. 4, 1960.

15) Panofsky, H. A. and G. W. Brier, Some Application of Statistics to Meteorology, Mineral Industries Continuing Education, College of Mineral Industries, The Pennsylvania State University, pp. 83, 84, 88, 1963.

16) Linke, F., Die nächtliche effektive Ausstrahlung unter verschiedenen Zenitdistanzen, Met. Zeits., Vol. 48, p. 25, 1931.

17) Thourel, L., The Antenna, John Wiley and Sons, Inc. New York, 1960.

18) Tiuri, M. E., Radio Astronomy Receivers, IEEE Transactions on Military Electronics, Vol. Mil-8, Nos. 3-4, July-October, 1964.

19) Colvin, R. S., A Study of Radio Astronomy Receivers, Stanford Electronics Laboratory Scientific Report No. 18, October, 1961.

20) Richer, K. A. and D. G. Bauerle, Near Earth Millimeter Wave Radiometer Measurements, Proceedings of the 1964 World Conference on Radio Meteorology, National Bureau of Standards, Boulder, Colorado.

21) Conway, W. H., and A. Mardon, Microwave Radiometers for Ocean and Weather Measurements, Proceedings of the Conference on Oceanography from Space, Woods Hole Oceanographic Institution, reference 65-10, 1965

22) Helliwell, R. A., Lecture notes for a course in ionospheric radio propagation, Stanford University, 1957.

23) Moreno, T., Microwave Transmission Design Data, Dover Publications, Inc., New York, 1948.

24) Jordan, E. C., Electromagnetic Waves and Radiating Systems, Prentice-Hall, Inc., 1950.

25) Beckman, P. and A. Spizzechino, The Scattering of Electromagnetic Waves from Rough Surfaces, The Macmillan Company, New York, 1963.

26) Venugopal, V. R., Meteorological Conditions and Radio Astronomy Observations at X-Band, J. Atms. Sci., Vol. 20, No. 5, September, 1963.

27) Porter, R. A., Significance of Radiative Sky Temperature in the Determination of the Apparent Temperatures of Materials, The Application of Passive Microwave Technology to Satellite Meteorology: A Symposium, The Rand Corporation, RM-3401, NASA, August, 1963.

28) Buettner, K. J. K., Regenortung von Wettersatelliten mit Hilfe von Zentimeterwellen, Naturwissenschaften, Vol. 50, No. 18, 1963.

29) Medhurst, R. G., Rainfall Attenuation of Centimeter Waves: Comparison of Theory and Measurement, IEEE Transactions on Atennas and Propagation, Vol. AP-B, No. 4, July, 1965.

30) Stogryn, A. P., Effect of Scattering by Precipitation on Apparent Sky Temperature in the Microwave Region, Space General Corporation, SGC 613TM-1, September 25, 1964.

31) Diermanjcan, D., Complete Microwave Scattering and Extinction Properties of Polydispersed Cloud and Rain Elements, The Rand Corporation, R-422-PR, December, 1963.

32) Rossby, S., Paper presented at the 1964 Western AGU Meeting, University of Washington, Seattle, Washington.

33) Kellogg, W. W., Buettner, K. J. K., and E. C. May, Meteorological Satellite Observation of Thermal Emission, The Rand Corporation, RM-4392-NASA, December, 1964.

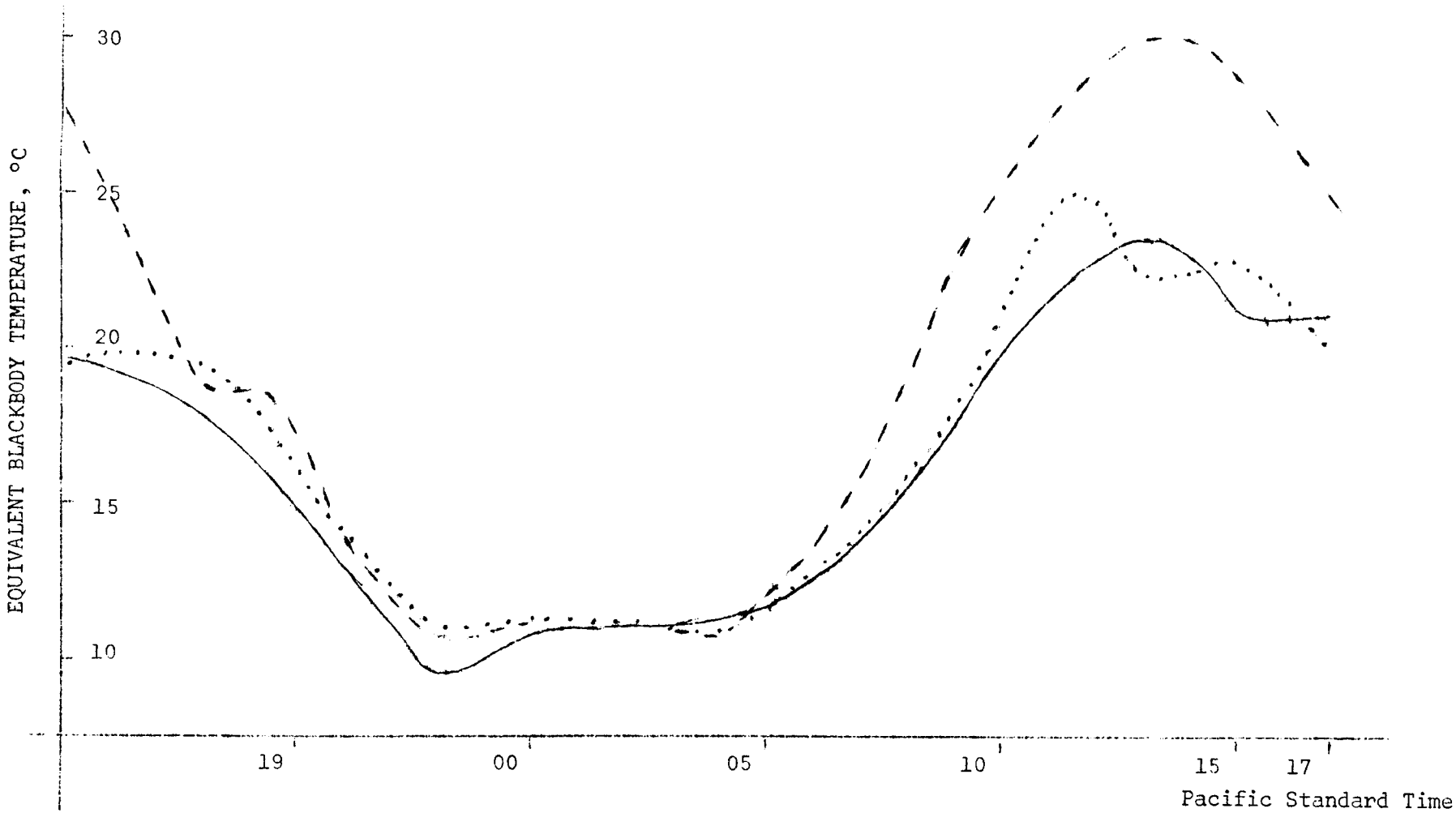

FIGURE 1. Radiative Temperatures measured at Stevens Canyon, July 15-16, 1965.

a) _____ low brush
b) . . . fir trees on lower slope of canyon
c) _ _ _ rock slide on lower slope of canyon

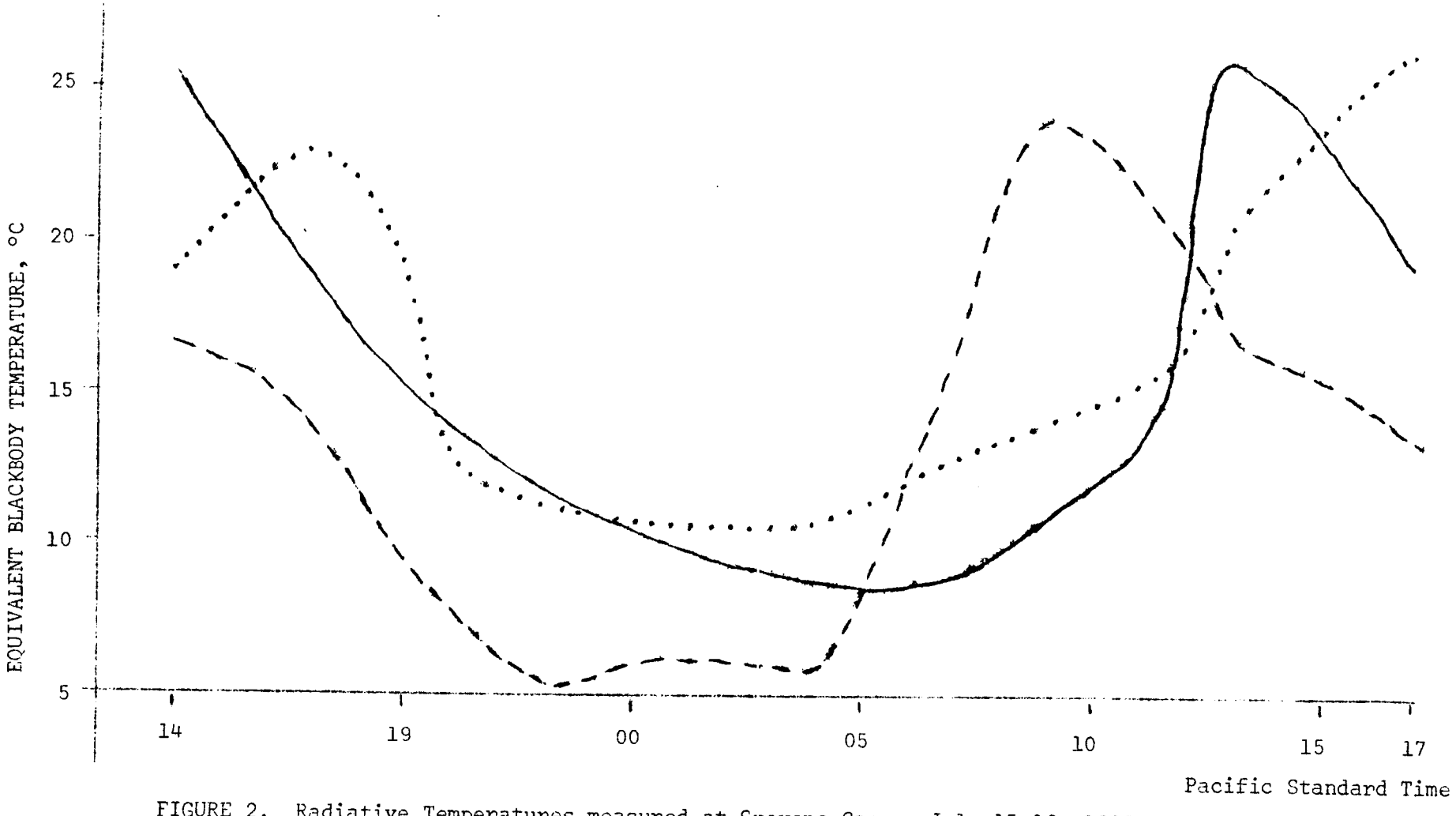

FIGURE 2. Radiative Temperatures measured at Stevens Canyon July 15-16, 1965.

a) . . . vertical gray rock face by road facing W.S.W.
b) _____ vertical gray rock face by road facing south
c) _ _ _ slide above river, facing N.E.

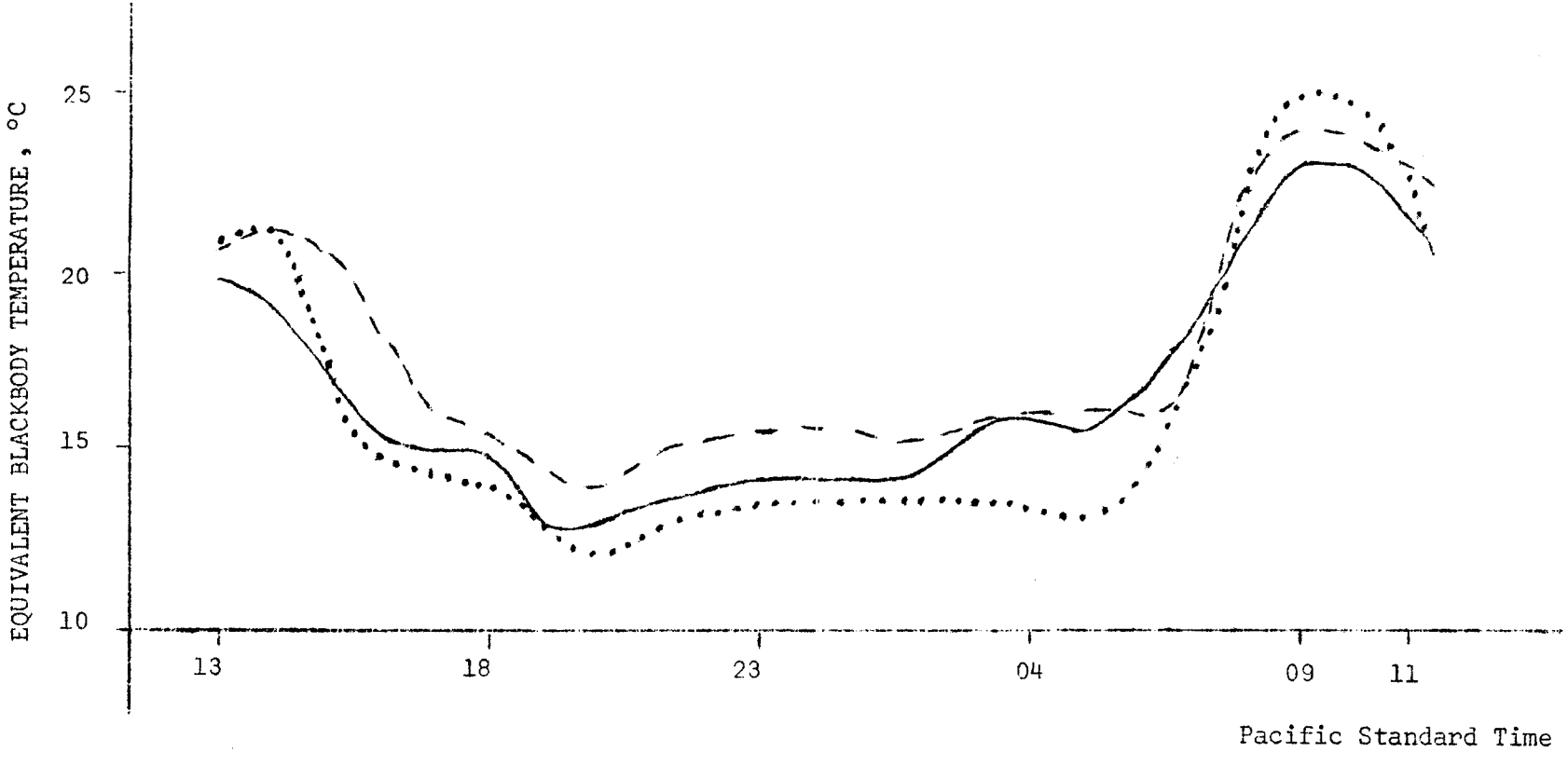

FIGURE 3. Radiative Temperatures measured at Ipsut Pass, August 16-17, 1965.

a) . . . green deciduous growth
b) _____ spruce thicket
c) _ _ _ darker spruce thicket

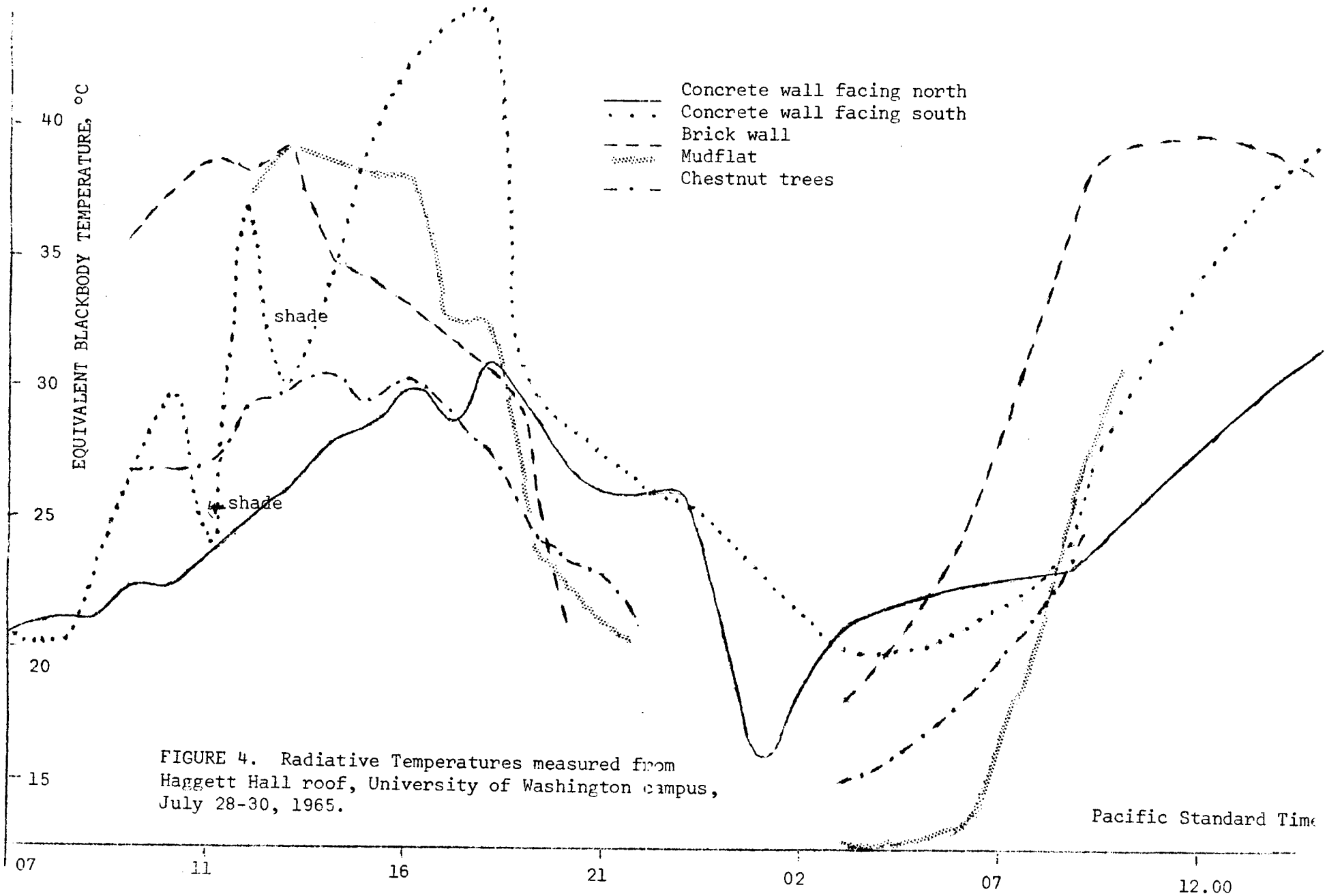

FIGURE 4. Radiative Temperatures measured from Haggett Hall roof, University of Washington campus, July 28-30, 1965.

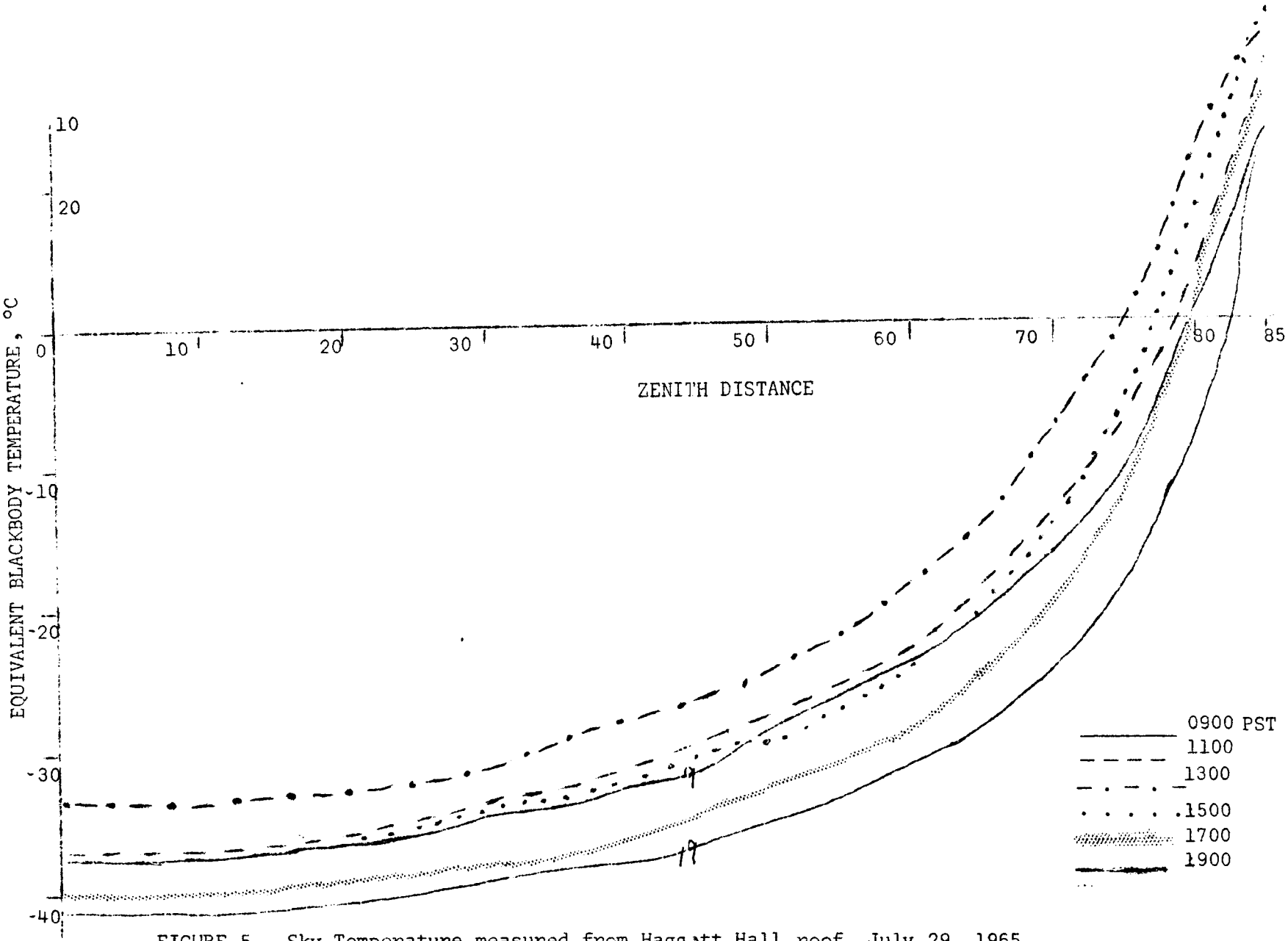

FIGURE 5. Sky Temperature measured from Haggett Hall roof, July 29, 1965.

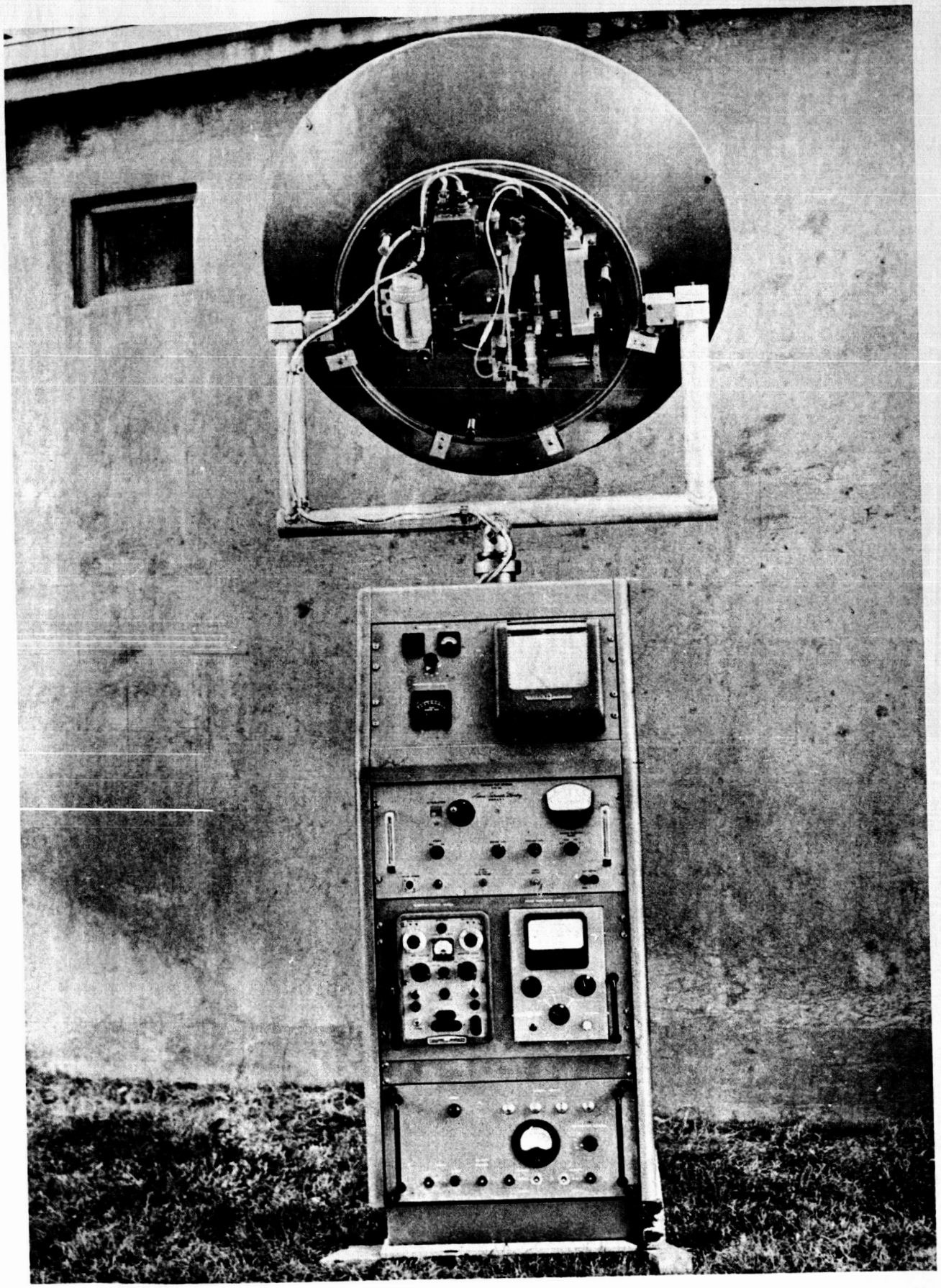

FIGURE 6

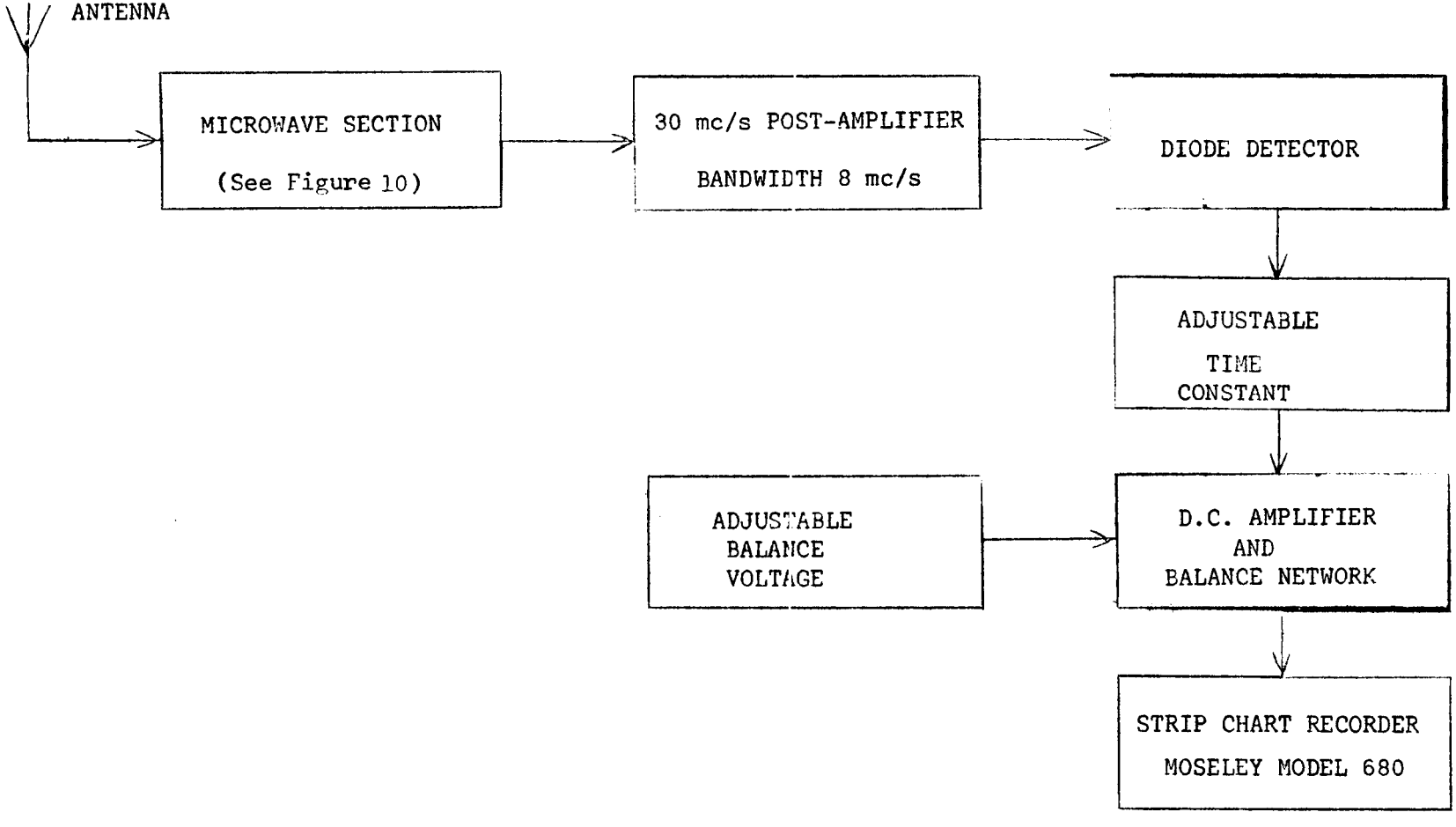
ANTENNA
MICROWAVE SECTION
(See Figure 10)
30 mc/s POST-AMPLIFIER
BANDWIDTH 8 mc/s
DIODE DETECTOR
ADJUSTABLE
TIME
CONSTANT
ADJUSTABLE
BALANCE
VOLTAGE
D.C. AMPLIFIER
AND
BALANCE NETWORK
STRIP CHART RECORDER
MOSELEY MODEL 680

FIGURE 7

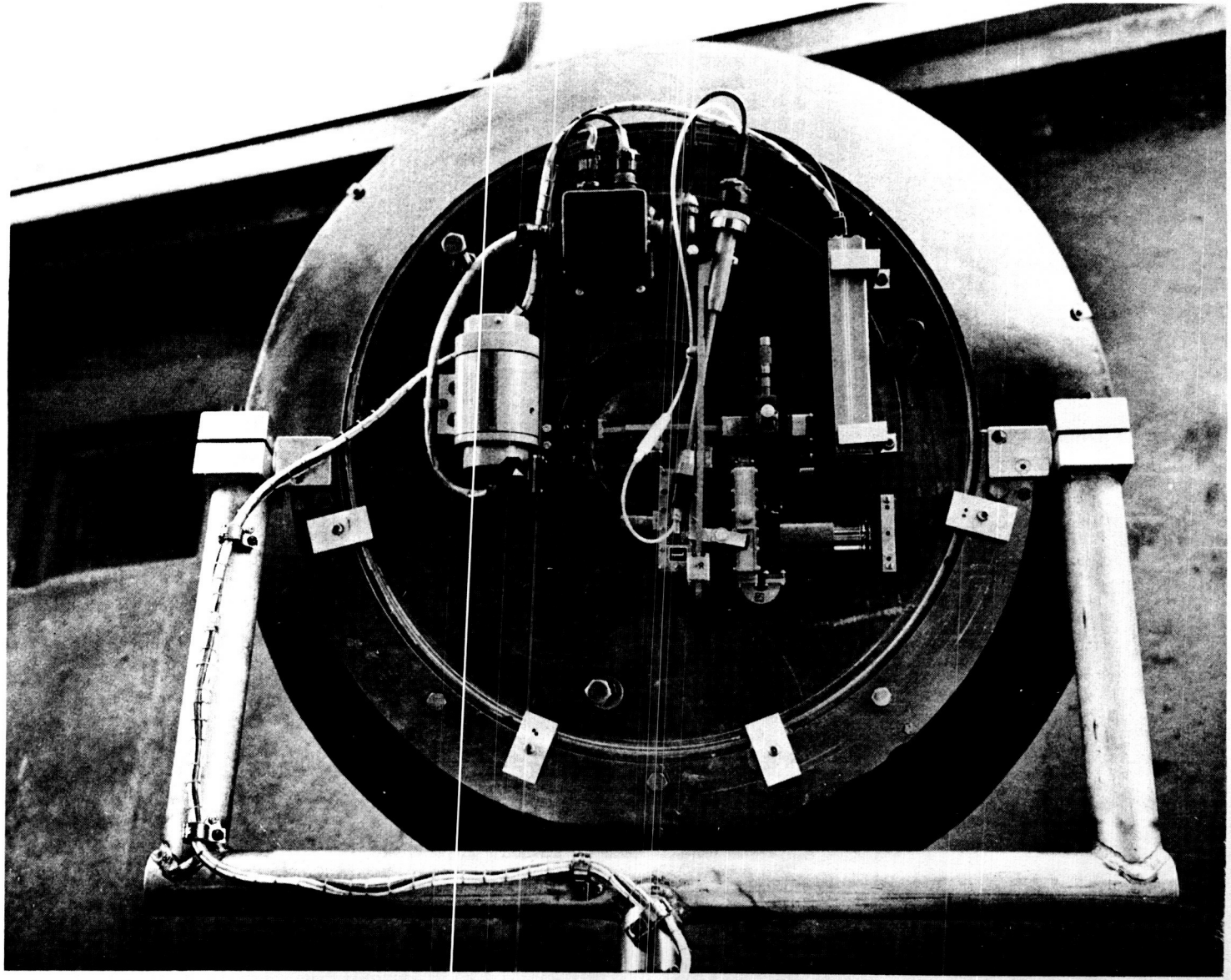

FIGURE 8

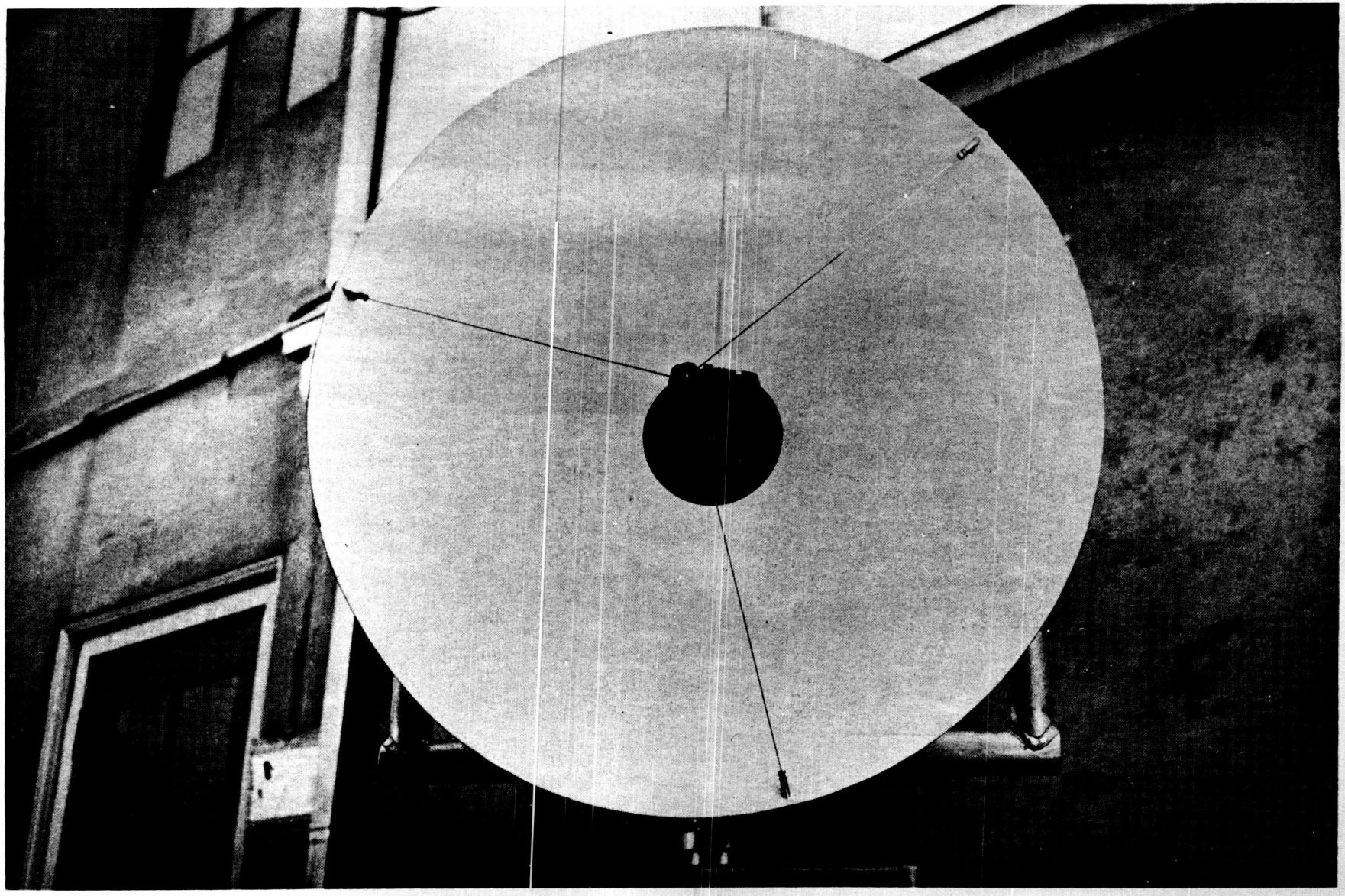

FIGURE 9

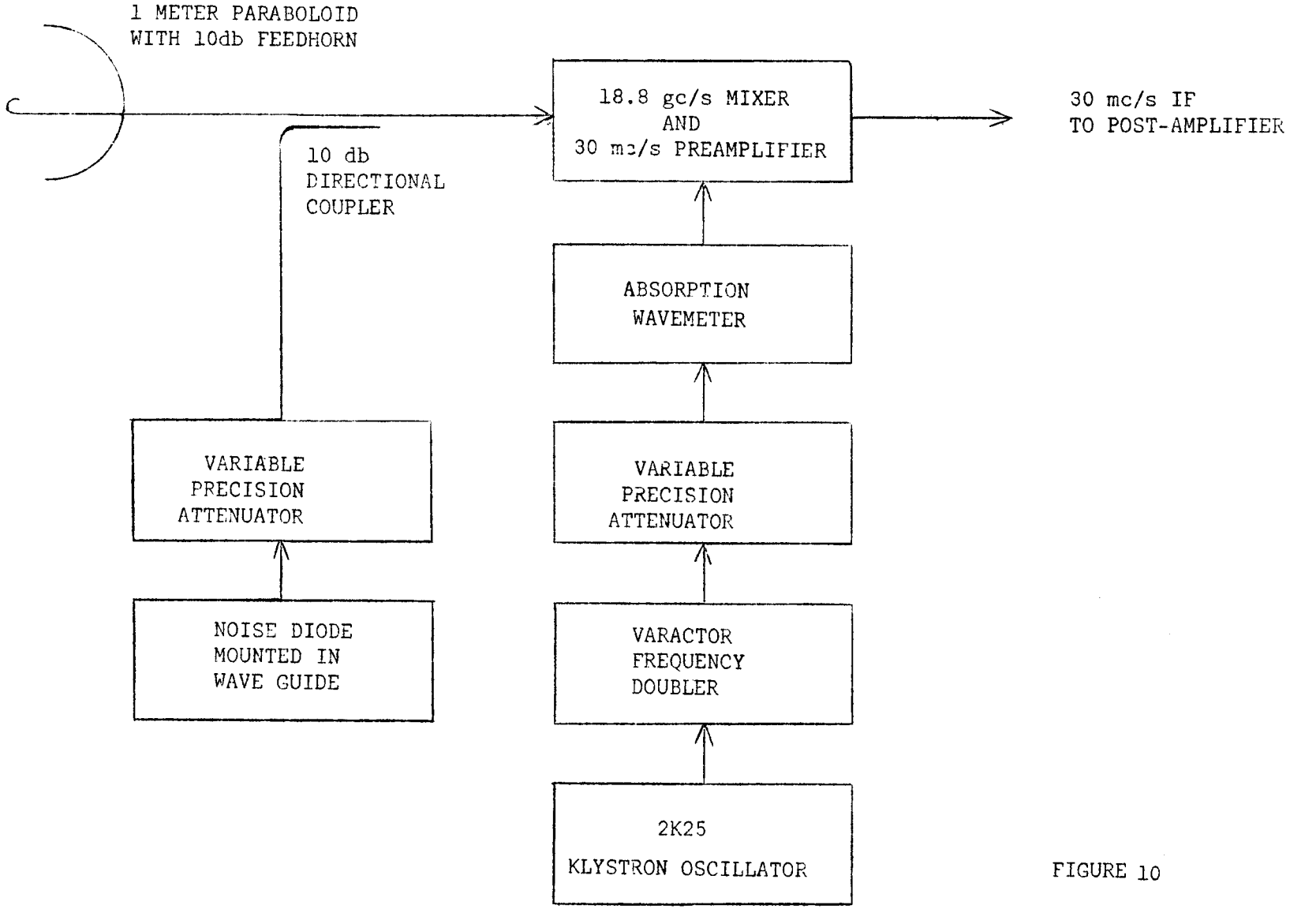
1 METER PARABOLOID
WITH 10db FEEDHORN
18.8 gc/s MIXER
AND
30 mc/s PREAMPLIFIER
30 mc/s IF
TO POST-AMPLIFIER
10 db
DIRECTIONAL
COUPLER
ABSORPTION
WAVEMETER
VARIABLE
PRECISION
ATTENUATOR
VARIABLE
PRECISION
ATTENUATOR
NOISE DIODE
MOUNTED IN
WAVE GUIDE
VARACTOR
FREQUENCY
DOUBLER
2K25
KLYSTRON OSCILLATOR

FIGURE 10

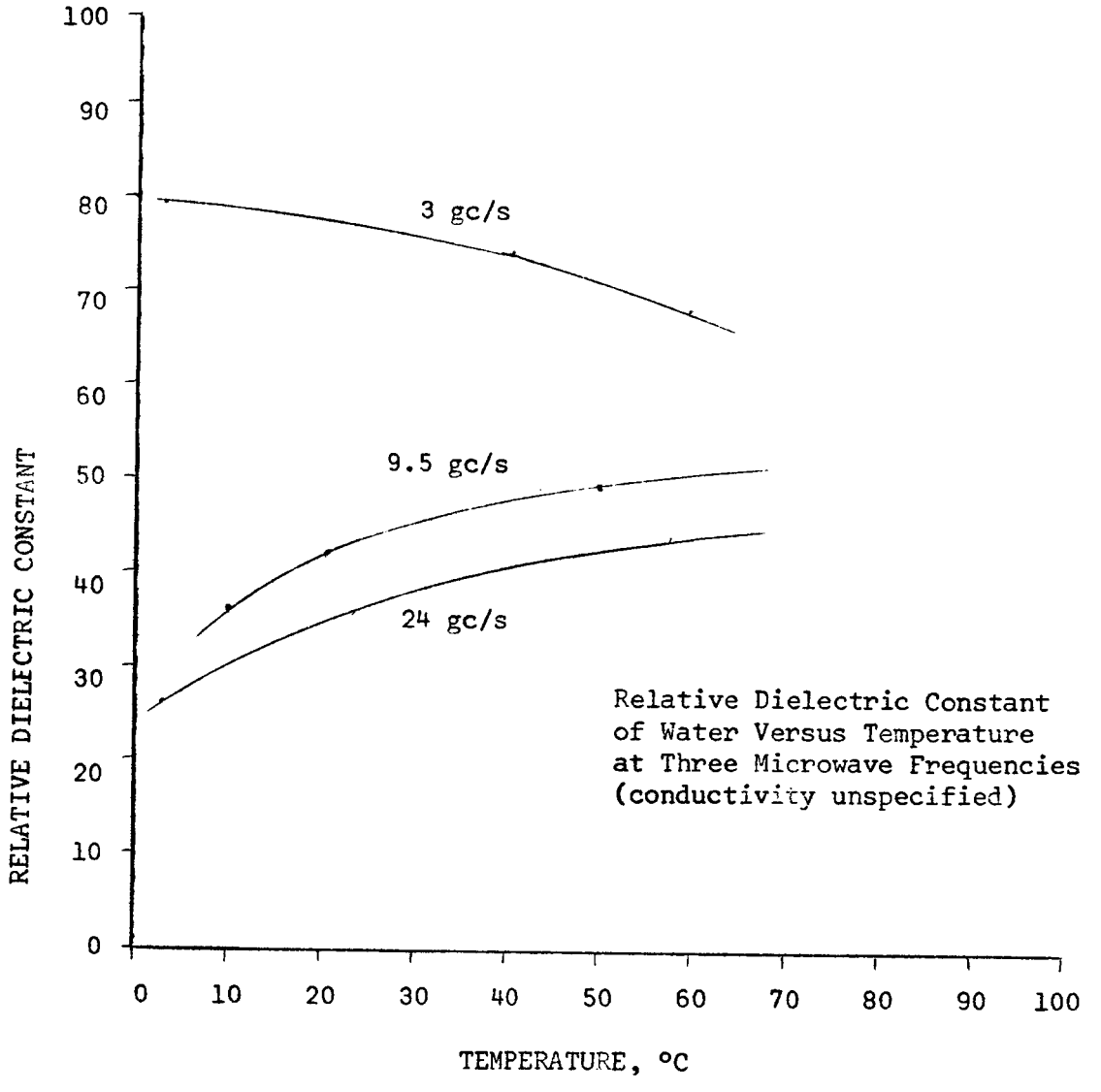

(Data taken from Moreno, 1948)

FIGURE 11

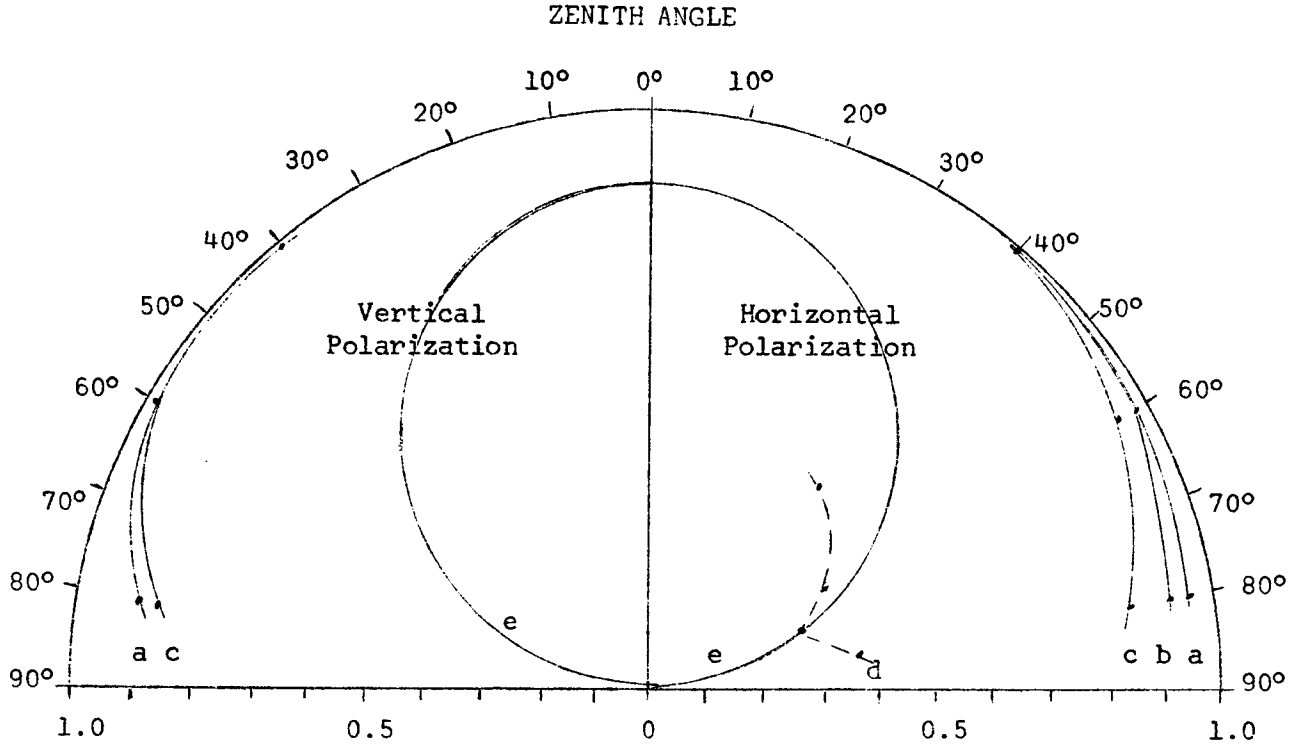

(Data taken from Richer and Bauerle, 1964, 35 gc/s)

Curve	Material
a	3" Grass
b	5" Marsh Weeds
c	Earth
d	Bay Water
e	Lamberts Law

FIGURE 12

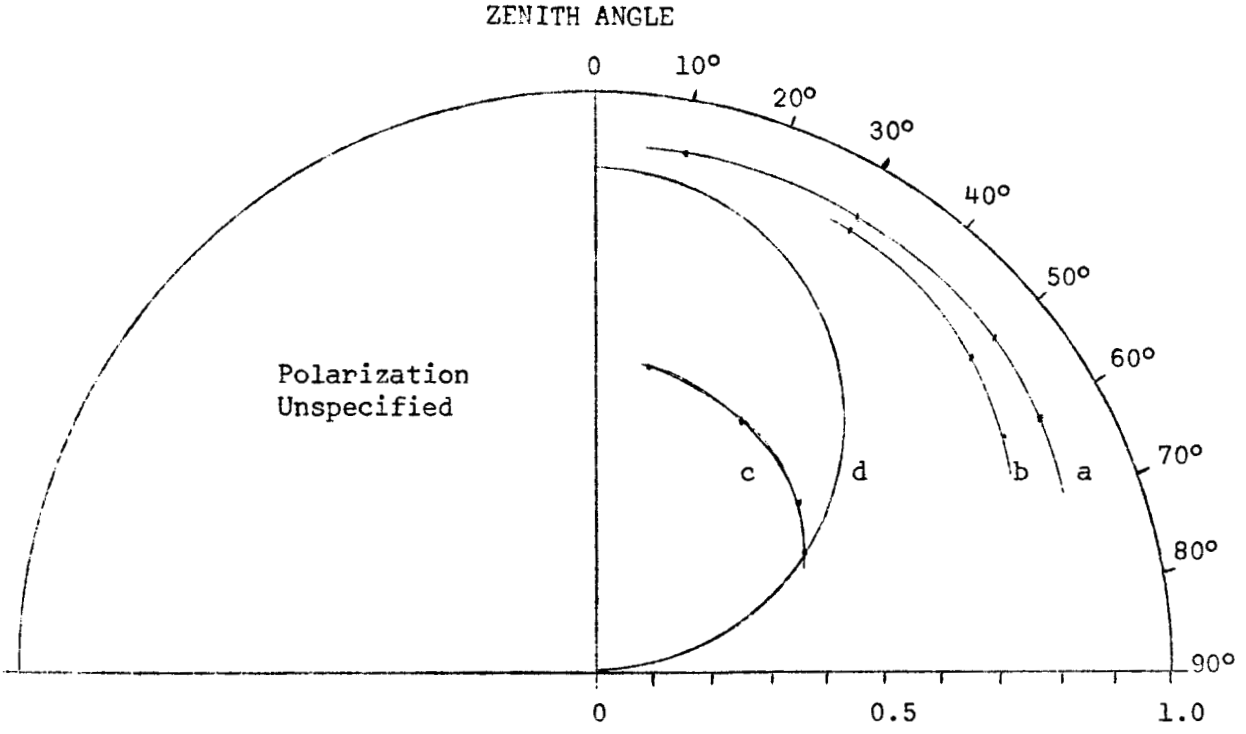

(Data taken from Conway and Mardon, 1965, 16 gc/s)

Curve	Material
a	Grass-bushes
b	Sand
c	Water (conductivity unspecified)
d	Lamberts Law

Note: These emissivities were calculated from apparent temperatures assuming thermometric temperature of 290°K.

FIGURE 13

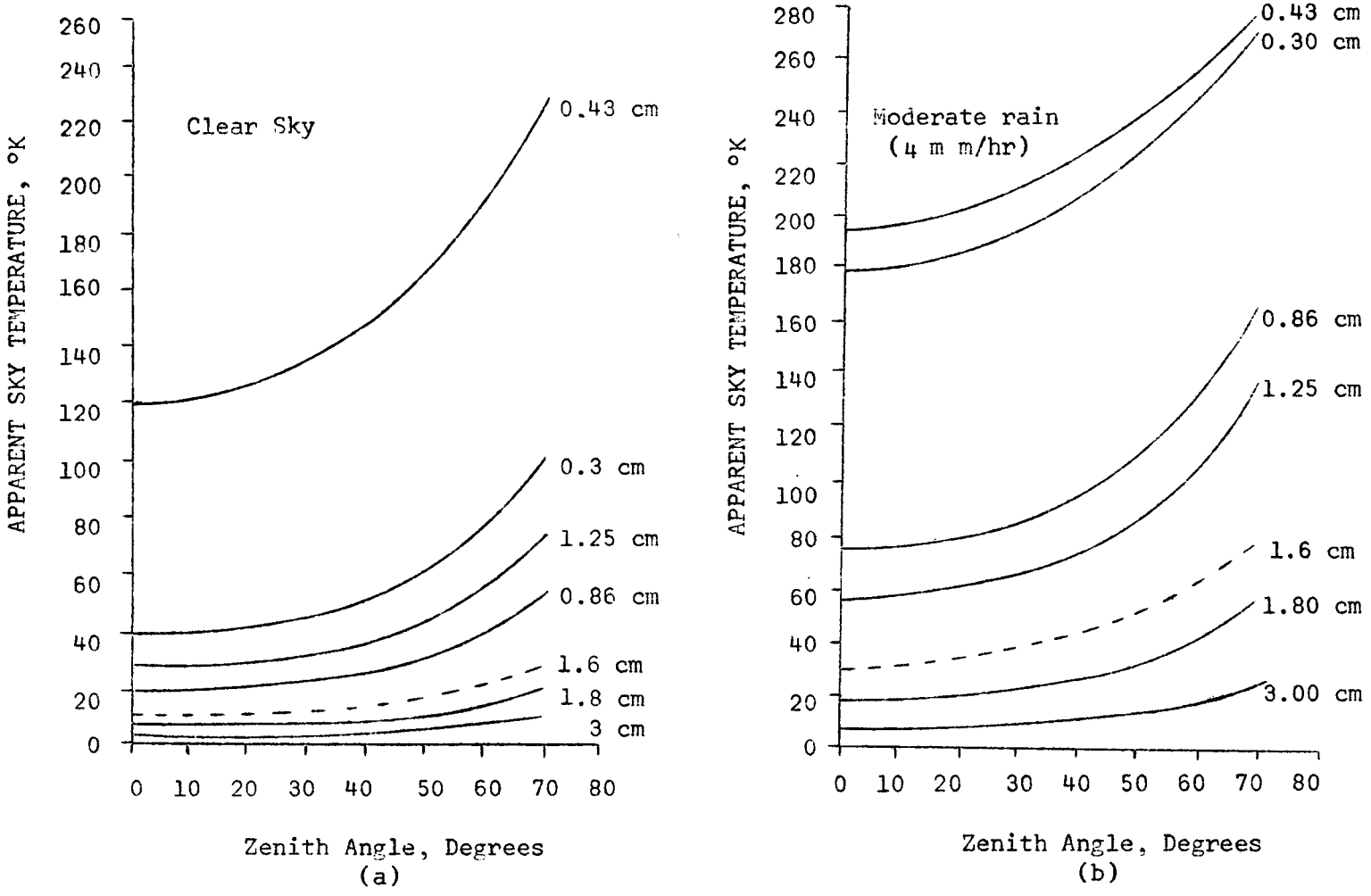
APPARENT SKY TEMPERATURE, °K
260
240
220
200
180
160
140
120
100
80
60
40
20
0
Clear Sky
0.43 cm
0.3 cm
1.25 cm
0.86 cm
1.6 cm
1.8 cm
3 cm
0 10 20 30 40 50 60 70 80
Zenith Angle, Degrees
(a)
APPARENT SKY TEMPERATURE, °K
280
260
240
220
200
180
160
140
120
100
80
60
40
20
0
Moderate rain
(4 m m/hr)
0.43 cm
0.30 cm
0.86 cm
1.25 cm
1.6 cm
1.80 cm
3.00 cm
0 10 20 30 40 50 60 70 80
Zenith Angle, Degrees
(b)

FIGURE 14

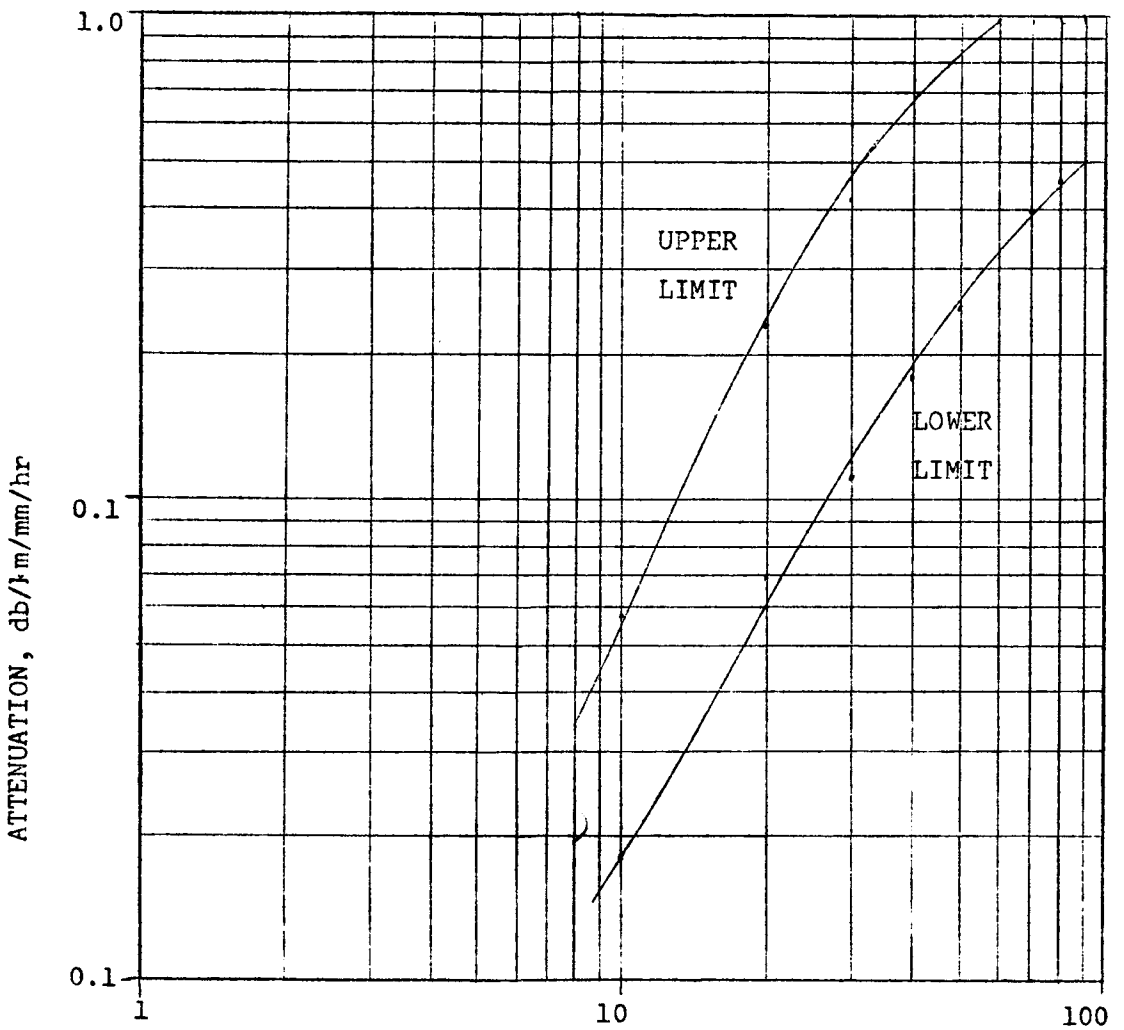

Frequency, gc/s

(After Medhurst, 1965)

FIGURE 15

Correction to the First Semi-Annual Report Contract NASA NSG-632 by K. J. K. Buettner, K. Katsaros and W. Kreiss: on page 6 there is a misprint. The "sand dunes of South Hanford" data in Table I is erroneous. The first line of sand dune emissivity should read 94.7 rather than 97.4.